Physical conditions and frictional properties in a slow slip event source region

A. F., Arnulf[1,*], J., Biemiller[1], L. Lavier[1], L. M. Wallace[2,1], D. Bassett[2], S. Henrys[2], I. Pecher[3], G. Crutchley[4], A. Plaza Faverola[5].

[1]Institute for Geophysics, Jackson School of Geosciences, University of Texas at Austin, Austin, Texas, 78758, USA.

[2]GNS Science, Lower Hutt, New Zealand.

[3]University of Auckland, Auckland, New Zealand.

[4]GEOMAR Helmholtz Centre for Ocean Research, Kiel, Germany.

[5] CAGE – Centre for Arctic Gas Hydrate, Environment and Climate, Department of Geosciences, UiT The Arctic University of Norway, Tromsø, Norway

Contact: Adrien F. Arnulf

[*]**Email: aarnulf@ig.utexas.edu**

Abstract:

Recent geodetic studies have shown that slow slip events can occur on subduction faults, including their shallow (< 15 km depth) parts where tsunamis are also generated. Although observations of such events are now widespread, the physical conditions promoting shallow slow-slip events remain poorly understood. Here, we use full waveform inversion of controlled-source seismic data from the central Hikurangi (New Zealand) subduction margin to constrain the physical conditions in a region hosting slow slip. We find that the subduction fault is characterized by compliant, overpressured and mechanically weak material. We identify sharp lateral variations in pore pressure, which reflect focused fluid flow along thrust faults and have a fundamental influence on the distribution of mechanical properties and frictional stability along the subduction fault. We then use high-resolution data-derived mechanical properties to underpin rate-state friction models of slow slip. These models show that shallow subduction fault rocks must be nearly velocity-neutral to generate shallow frictional slow slip. Our results have implications for understanding fault loading processes and slow transient fault slip along megathrust faults.

In the last two decades, one of the most important advances in earthquake science has been the discovery of a spectrum of transient slip-phenomena, such as slow slip-events (SSEs), which occupy the continuum between fast, seismic slip (seconds) through to steady, aseismic creep at plate motion rates. SSEs can last days to years and are widely viewed as manifestations of conditional fault zone stability, in the transition from stick-slip (velocity weakening) behavior to stable sliding (velocity strengthening) behavior[1,2]. However, the underlying physical mechanism for episodic, aseismic slip remains unclear and there are a number of parameters including rock physical properties, low effective stress linked to elevated pore-fluid pressure, and structural and/or lithological heterogeneities that may give rise to this phenomenon[2-5]. Better constraints on the structural and physical conditions within the conditionally stable, SSE-hosting region of megathrust faults is therefore crucial for understanding mechanisms of slow transient fault slip, and their relationship to damaging seismic slip events.

Seismic attributes[6,7] and velocity images[8-11] from active-source seismic data provide an opportunity to infer the elastic properties and stress state of the plate interface and overlying accretionary wedge, particularly for shallow (<15 km deep) SSE regions where such methods can provide high-resolution results. SSEs at the central and northern Hikurangi subduction margin (HSM) occur at <15km depth[12,13], placing the SSE source within range of modern seismic imaging techniques such as full waveform inversion (FWI)[14], from which high-resolution physical models of the Earth can be inferred[15-16].

In 2005, a regional grid of ~2800-line km of multichannel seismic (MCS) data (survey 05CM) was collected along the HSM[17] (Fig. 1). Here, we derive elastic models of the central HSM, through a combination of traveltime tomography and elastic FWI of downward extrapolated MCS data[18-20], along profile 05CM-38 (Methods, Figs. 2 and 3, Extended Data Figs. 1, 2, 3, 4 and 5, Supplementary Videos 1, 2 and 3). This profile spans the southern end of a region of shallow slow slip, within the along-strike transition from an interseismically locked megathrust in the south to an aseismically creeping megathrust in the north[13]. Well-characterized SSEs typically occur here every 5 years, lasting 2-3 weeks, at <15 km below the seafloor[13,21-22]. This region also hosted an SSE that was dynamically triggered by the 2016 Mw 7.8 Kaikoura earthquake, over 250 km away[21-22]. Following FWI of the MCS data, we estimate pore pressure and in-situ stresses within the accretionary wedge by applying calibrated empirical relations between compressional P-wave velocity, porosity and effective stress[10] (Methods). We then use the physical parameters constrained by FWI to construct rate-state friction (RSF) models[23] of the shallow HSM, to investigate how upper plate strength and pore fluid pressure influence slow-slip fault behavior. This study represents the first time that highly detailed data on physical properties have been utilized to constrain such models.

Geological Setting.

The HSM accommodates westward subduction of the Pacific Plate beneath the East Coast of New Zealand's North Island. In this area, the subducting Pacific Plate is composed of the Hikurangi Plateau, a Cretaceous Large Igneous Province[24]. A broad sedimentary wedge has been accreted outboard of an actively deforming foundation of pre-subduction Cretaceous and Paleogene marine formations that emerge above sea-level along the East Coast of North island[25,26] (Fig 2). The incoming plate sequence is comprised of volcanics and volcaniclastics of the Hikurangi Plateau and sedimentary sequences overlying the Plateau (Fig. 2). Along our seismic transect, subducted unit 4 is interpreted as a sequence of chalks and mudstones, while above reflector R7, unit 3 is inferred to consist of nannofossil chalks interbedded with tephras and clays[25]. Reflector R5B corresponds to a major regional unconformity, overlain by a >3 km thick, shale-rich (53–80%) turbidite sequence and slope basin sediments (units 0 to 2; stratigraphic nomenclature from ref.[26]; Fig. 2). The subduction fault lies between units 3 and 4 in this region (thick dashed line, Figs 2 and 3).

Structural and physical characteristics of the HSM

We perform an advanced inversion and analysis of 12-km-long-offset seismic reflection data across the central HSM using elastic time-domain FWI and reverse time migration (RTM, Methods). Our results provide high-resolution models of elastic properties (i.e. P-wave velocity, ratio of P- and S-wave velocities, Lamé parameters) that show improve correlations with lithostratigraphic interpretations (Figs. 2 and 3, Extended Data Figs. 1–2, Supplementary Figs. 1, 2), compared to earlier analyses[17,27]. The P-wave velocity model is then used to derive wedge mechanical properties and stress state (e.g. pore fluid pressure, Fig. 3, Methods).

Overall, this section of margin wedge is characterized by P-wave velocities ranging from ~1.6 km/s at the seafloor to a maximum of ~4.75 km/s at 7.5 km depth. Below the bottom simulating reflector (BSR) and in the vicinity of the subduction fault (Figs. 2 and 3), velocities strongly deviate from a normal compaction trend and suggest porosity preservation associated with the presence of free gas and/or pressurized fluids[27]. Within the margin wedge, bulk moduli range from ~5 GPa at the seafloor to 17–32 GPa at ~7.5 km depth. Similarly, the shear modulus of the upper plate ranges from <1 GPa at the seafloor to 6–14 GPa near the decollement (Fig. 3, Extended Data Figs. 6-7). We estimate uncertainties in the final elastic parameters to be at most ±20% (Extended Data Fig. 7). Low effective stress (<40 MPa) conditions are present throughout the wedge, linked to elevated Hubbert-Rubey pore fluid pressure ratio (λ^*, Methods) values up to 0.89 along the entire section (Fig. 3), which testify to the widespread overpressured nature of the offshore central HSM. This last observation is in good agreement with the widespread evidence of low permeability, clay-rich formations, acting as effective seals to vertical fluid flow[28].

From east to west, we identify four structural domains for the margin wedge (Fig. 2). The active protothrust zone[29] is characterized by low-velocity sediments and high pore-fluid pressures in the lower half of the section (units 3 and 4). Progressing landward, the outer and inner Neogene accretionary wedges are differentiated by the degree of macro-scale deformation and shortening, ~5% and ~24% respectively. ~65 km from the trench, a westward increase in velocity (+0.5 km/s, at ~3.5 km depth) marks the boundary between the Neogene accretionary wedge and the deforming foundation of pre-subduction, Cretaceous to Paleogene rocks (Fig. 2, Extended Data Fig. 8). The deforming foundation is characterized by stiffer material and likely acts as a mechanical backstop behind the accretionary wedge. A change in mechanical and frictional properties across this major regional boundary[27] is also suggested from the abrupt westward increase in local seismicity[22] (Figs. 1 and 2).

We find that distribution of pore fluid pressure (Fig. 3e) within the outer forearc is closely tied to lithostratigraphy and that it correlates positively with the reflectivity intensity of our RTM image (Fig. 2, Supplementary Fig. 1). Within the turbidite section, variations in pore fluid pressure ratio (λ^*) between unit 1 ($\lambda^* = 0.5 – 0.8$) and unit 2 ($\lambda^* = 0.4\pm0.1$) likely reflect variations in clay content and grain size[30]. In the vicinity of the subduction fault, low seismic velocities within the Hikurangi Plateau cover sequence (unit 4) likely suggests high pore fluid pressure and under-consolidation of subducted sediments[9,10,31], and we estimate $\lambda^* = 0.5 – 0.89$. In detail, these low-velocity zones are stratified, suggesting that sedimentary layering produces permeability anisotropy that guides fluid flow laterally along preferential strata, increasing the drainage path length and therefore affecting pore fluid pressure and effective stress[32,33] (Fig. 4). Pronounced, ~100 m vertical variations in elastic properties, ratio of P- and S- wave velocities and effective stress within units 3 and 4 (Fig. 3), may reflect focused flow and storage of pressurized fluids along higher permeability sedimentary strata.

Along the entire transect, sharp lateral transitions in P-wave velocity, elastic properties and estimated pressure regimes across the main thrust faults suggest a clear lateral partitioning of the margin into thrust blocks of distinct mechanical properties. Fault compartmentalization is particularly marked across the main thrust faults within the

Neogene wedge, which form low-velocity, low-rigidity, pressurized conduits of potentially higher fault-permeability and likely play a key role in fluid drainage (Fig. 3h). Predicted pore fluid pressure ratios within subducted strata are lower where footwall faults (group C, Figs. 2, 3 and 4) connect with large thrust faults in the wedge that branch toward the seabed (group A, Figs. 2, 3 and 4). We note that thrust faults terminating deeper beneath the seabed (group B, Figs. 2, 3 and 4) appear less effective at relieving fluid-overpressure at depth. From these observations, we identify two very compliant and highly overpressured regions (regions I and III, Figs. 2, 3 and 4, Extended Data Fig. 6) surrounding a stiffer portion of the subduction fault where elastic moduli increase by ≥40%, and fluid overpressure reduces by up to 35% (region II, Figs. 2, 3 and 4, Extended Data Fig. 6).

Implications for fault stability and slow-slip

Modeled mechanisms for aseismic creep transients include mixed brittle-ductile deformation[34,35], unstable aseismic slip on faults governed by rate-and-state friction (RSF) with conditional frictional stability parameters, near-lithostatic pore-fluid pressures, or heterogeneous distributions of rate-weakening and rate-strengthening material[2,4,5,36-40]. Rate-state frictional stability of a material is described by the experimentally determined parameters a and b: materials with b-a < 0 are velocity-strengthening, where an increase in slip velocity causes an increase in friction; materials with b-a > 0 are velocity-weakening, where increasing slip velocity leads to a drop in friction and potentially unstable seismic slip. SSE conditions in RSF models are broadly inferred from geophysical and numerical evidence[2,36,37] or iterative parameter searches that select parameter values to recreate SSE characteristics like recurrence interval and/or duration[41]. However, without data-constrained predictions of pore pressure and rigidity it is difficult to assess whether these model-inferred properties are physically realistic characterizations of subduction faults. Our FWI seismic images constrain the physical properties of a shallow SSE source at higher resolution than has previously been possible, thus providing the first opportunity to construct RSF models using high-resolution data-constrained physical parameters. These data show two prominent differences between the shallow central HSM and previously modeled SSE conditions. First, our data suggest that although pore-fluid pressure on the decollement is overpressured ($\lambda^* \sim 0.52 – 0.82$), it is not nearly as high as the near-lithostatic values assumed in other SSE modeling studies (λ^* up to 0.999 in ref.[39], 0.998 in ref.[41]). However, it is worth noting that from a methodological perspective, it remains virtually impossible to reject the presence of highly pressurized material confined in thin layers below the resolution dictated by the data (i.e. in layers <70 m thick, Methods). The λ^* values we obtain for central HSM are comparable to those estimated for the offshore Nankai trough[42], also a region of shallow slow slip[43]. Second, elastic FWI shows that shear moduli in the upper plate (<1 to 6–14 GPa) are significantly lower than the 25-50 GPa that have typically been used in SSE models.

Using the shallow elastic properties and effective normal stress constrained by FWI, we find that RSF numerical experiments with commonly used values of $b\text{-}a$ (0.001 – 0.004) and d_c (2 – 10 mm) struggle to reproduce the slip style, durations and recurrence intervals of central Hikurangi SSEs ($(b\text{-}a)/d_c \sim 0.1 - 2\ m^{-1}$, Fig. 5, Extended Data Fig. 9). These models cannot fully reproduce the observed 5-year recurrence interval of central Hikurangi SSEs, but models with reduced $(b\text{-}a)/d_c$ (0.075 – 0.0125 m^{-1}) approach the observed recurrence intervals and magnitudes (Fig. 5b). For example, Figure 5 shows a comparison of the transient aseismic slip modeled with parameters tuned to reproduce SSEs in other studies (Fig. 5a, parameters from ref.[41]) and the predominantly seismic slip modeled using shear moduli and effective normal stress from our FWI results along with b-a (0.001) and d_c (8 mm) values at the lowest and highest (respectively) ends of the range of values used in previous studies[39-41] (Fig. 5b). In Fig 5b, slow-slip (upper panel) occurs updip of a deeper seismogenic region (lower panel). Fault stability in RSF continuum models is primarily determined by the effective fault stiffness ratio W/h*, where W is the width of the velocity-weakening patch and h* is the critical cell size to generate unstable slip events. This fault stiffness ratio depends on shear modulus, Poisson's ratio, effective normal stress, RSF parameters ($b\text{-}a$ and d_c) and fault geometry. By implementing the elastic properties from FWI at central HSM, we find that the fault instability parameter W/h^* increases by up to two orders of magnitude relative to those of previous studies[37,39,41], thereby significantly limiting the range of the RSF parameter $(b\text{-}a)/d_c$ that allows transient aseismic slip events ($(b\text{-}a/d_c)$ < 0.325 m^{-1}; b-a < ~0.00026 for d_c ~ 8 mm, Fig. 5c). In particular, the higher effective normal stresses inferred by FWI tend to drive the deeper portion of the fault towards seismic instability (Fig 5b, lower panel). The blue envelope in Fig 5c shows the upper and lower bounds of W/h* stability relationships associated with a range of FWI-derived near-fault shear moduli (6-14 GPa; Fig 3c; Extended Data Figs. 6 and 9) and effective normal stresses (10-30 MPa; Fig 3f; Extended Data Fig. 9). Although uncertainties in the FWI-derived mechanical properties are smaller than this range, this envelope shows that 30-100% variations in these parameters yield similarly limited ranges of (b-a)/d_c for frictional slow-slip, demonstrating that this result is largely insensitive to FWI uncertainties.

One explanation for this departure is that b-a, the frictional property that determines velocity-weakening or velocity-strengthening behavior, is nearly zero through most of the SSE patch. This conclusion is potentially unsatisfying[44], as it has been argued that SSE-hosting subduction zone faults worldwide would be unlikely to share such specific frictional conditions. However, the near-velocity-neutral b-a values (b-a < ~0.001) required for slow-slip in our Hikurangi RSF models are remarkably similar to experimentally determined values (b-a ≤ 0.0015) for HSM sediments at plate tectonic strain rates[45]. Additionally, recent plate-rate laboratory experiments revealed near-velocity-neutral frictional slow-slip behavior in a wide variety of shallow fault gouges, suggesting that strain rates consistent with steady plate motion may lead to lower magnitude b-a than previous experiments have reported[45,46] and such low values may in fact be common. Alternatively, traditional RSF laws may not capture all of the mechanical processes responsible for shallow slow-slip[47]. For example, recent models[47] show that newly developed friction laws with slip-rate-dependent RSF parameters produce the wide range of slow-slip behavior observed in nature over a broader range of mechanical conditions than traditional RSF laws. Mechanically, these studies imply that subduction fault rocks may weaken and slip unstably at sub-seismic slip rates, but rapidly restrengthen and arrest unstable slip as slip rates approach earthquake velocities. The physical mechanisms underlying rate-dependent frictional stability are not yet fully resolved, but may involve increased dilation-hardening as slip accelerates to near-seismic rates.

Additionally, heterogeneity of fault friction[4] or effective normal stress[39,48] may reduce the effective size of the potentially unstable fault patch. Effective normal stress variations, such as those observed here related to drainage of fluids by thrust fault branching from the shallow subduction interface (Figs. 2, 3 and 4), have been shown to segment slow-slip in RSF models by creating barriers to unstable slip propagation[39,48]. Indeed, we find that barriers to slow-slip propagation in our FWI-constrained RSF models localize in regions with locally high upper plate shear modulus or sharp effective normal stress gradients (Fig 3g; Extended Data Fig. 10). Homogeneously distributed slow-slip segmentation arises spontaneously in our homogeneous property models (Extended Data Fig. 10), as has been reported in previous studies[39,48], but only models with heterogeneous shear moduli and effective normal stress show persistent localized segmentation over hundreds of slip cycles (Extended Data Fig. 10b,c). Abundant microseismicity downdip of the slow-slip region[13] (Fig. 1) may reflect similar fault-slip segmentation due to fault-controlled fluid compartmentalization, upper plate elastic and hydrogeologic properties (Fig. 4), or meter to tens of meters-scale variations in rigidity or fault geometry producing small, isolated unstable fault patches. Finally, it is important to note that time-variable physical processes may cause fault stability to change over time, as would be expected if SSEs occur in response to pore fluid overpressures gradually accumulating through the inter-event period[49,50].

Advanced seismic imaging offers unique quantitative constraints on the physical properties of the megathrust and overriding accretionary wedge over large areas, giving insight into the physical controls on shallow megathrust slip behaviors[11,15-16]. Along the central HSM, we find that the subduction fault is characterized by compliant, overpressured and mechanically weak material with marked variations along dip (i.e. regions with contrasting elastic and possibly frictional properties). We observe a strong contrast in predicted pore pressure across thrust faults as well as across the subduction thrust suggesting fault compartmentalization within the wedge and poorly-drained conditions beneath the decollement. Thrust faults act as conduits for fluids, locally reducing fluid pressure where these faults intersect the megathrust and creating meter-to-kilometer-scale heterogeneities in effective normal stress that may control fault slip stability and/or segmentation. We show that RSF models using FWI-constrained physical properties of the shallow central HSM are unable to reproduce slow slip behavior unless the fault is nearly velocity-neutral ($b-a < 0.001$) or overpressured beyond the level suggested by these data. This suggests that either shallow subduction zone fault rocks are nearly velocity-neutral at plate tectonic loading rates or that a more complex process such as time-dependent fault pressurization[47] may be responsible for observed shallow SSEs.

References:

1. Scholz, C. H. The Mechanics of Earthquake and Faulting, Cambridge Univ. Press, New York (1990).

2. Liu, Y., & Rice, J. R. Spontaneous and triggered aseismic deformation transients in a subduction fault model, *J. Geophys. Res.* **112**, B09404, doi:10.1029/2007JB004930 (2007).

3. Audet, P., Bostock, M. G., Christensen, N. I. & Peacock, S. M. Seismic evidence for overpressured subducted oceanic crust and megathrust fault sealing. *Nature* **457**, 76-78 (2009).

4. Skarbek, R. M., Rempel, A. W. & Schmidt, D. A. Geologic heterogeneity can produce aseismic slip transients, *Geophys. Res. Lett.* **39**, L21306, doi:10.1029/2012GL053762 (2012).

5. Saffer, D. M., & Wallace, L. M. The frictional, hydrologic, metamorphic and thermal habitat of shallow slow earthquakes, *Nat. Geosci.* **8**(8), 594–600, doi:10.1038/ngeo2490 (2015).

6. Nedimovic, M. R., Hyndman, R. D., Ramachandran, K. & Spence, G. D. Reflection signature of seismic and aseismic slip on the northern Cascadia subduction interface. *Nature* **424**, 416-419 (2003).

7. Calvert, A. J. Seismic reflection imaging of two megathrust shear zones in the northern Cascadia subduction zone. *Nature* **428**, 163-167 (2004).

8. Calvert, A. J., Preston, L. A. & Farahbod, A. M. Sedimentary underplating at the Cascadia mantle-wedge corner revealed by seismic imaging. Nature Geoscience 4, 545-548 (2011).

9. Crutchley, G. J., Klaeschen, D. Henrys, S. A., Pecher, I. A., Mountjoy, J. J. & Woelz, S. Subducted sediments, upper-plate deformation and dewatering at the New Zealand's southern Hikurangi subduction margin. *Earth and Planetary Science Letters* **530**, https://doi:org/10.1016/j.epsl.2019.115945 (2020).

10. Han, S., Bangs, N. L., Carbotte, S. M., Saffer, D. M. & Gibson, J. Links between sediment consolidation and Cascadia megathrust slip behavior, *Nat. Geosci.* **10**, 954-959 (2017).

11. Sallares, V. & Ranero, C. R. Upper-plate rigidity determines depth-varying rupture behavior of megathrust earthquakes. *Nature* **576**, 96-101 (2019).

12. Wallace, L.M., Webb, S.C., Ito, Y., Mochizuki, K., Hino, R., Henrys, S., Schwartz, S.Y. & Sheehan, A.F. Slow slip near the trench at the Hikurangi subduction zone, New Zealand. *Science* **352**(6286):701–704. https://doi.org/10.1126/science.aaf2349 (2016).

13. Wallace, L. M., Beavan, J., Bannister, S. & Williams, C. Simultaneous long-term and short-term slow slip events at the Hikurangi subduction margin, New Zealand: Implications for processes that control slow slip event occurrence, duration, and migration, *J. Geophys. Res.* **117**, B11402, doi:10.1029/2012JB009489 (2012).

14. Tarantola, A. A strategy for nonlinear elastic inversion of seismic reflection data. *Geophysics* **51** (10), 1893-1903 (1986).

15. Kamei, R., Pratt, R. G. & Tsuji, T. Waveform tomography imaging of a megasplay fault system in the seismogenic Nankai subduction zone. *Earth and Planetary Science Letters* **317-318**, 343-353 (2012).

16. Qin, Y., & Singh, S. C. Insight into frontal seismogenic zone in the Mentawai locked region from seismic full waveform inversion of ultralong offset streamer data. *Geochemistry, Geophysics, Geosystems* **19**, 4342–4365. https://doi.org/10.1029/2018GC007787 (2018).

17. Barker, D., Sutherland, R., Henrys, S. & Bannister, S. Geometry of the Hikurangi subduction thrust and upper plate, North Island, New Zealand. *Geochem. Geophys. Geosyst.* **10**, Q02007. http://dx.doi.org/10.1029/2008GC002153 (2009).

18. Arnulf, A. F., Singh, S., Harding, A., Kent, G., & Crawford, W. Strong seismic heterogeneity in layer 2a near hydrothermal vents at the mid-atlantic ridge. *Geophysical Research Letters* **38** (13), (2011).

19. Arnulf, A. F., Harding, A. J., Singh, S. C., Kent, G. M. & Crawford, W. C. Nature of upper crust beneath Lucky Strike volcano using elastic full waveform inversion of streamer data. *Geophysical Journal International* **196** (3), 1471-1491 (2013).

20. Harding, A. J., Arnulf, A. F. & Blackman, D. K. Velocity structure near IODP Hole U1309D, Atlantis Massif, from waveform inversion of streamer data and borehole measurments. *Geochemistry Geophysics Geosystems* **17** (6), 1990-2014 (2016).

21. Wallace, L.M., Hreinsdóttir, S., Ellis, S., Hamling, I., D'Anastasio, E. & Denys, P. Triggered Slow Slip and Afterslip on the Southern Hikurangi Subduction Zone following the Kaikoura Earthquake. *Geophys. Res. Lett.* **45**, 4710-4718, https://doi.org/10.1002/2018GL077385 (2018).

22. Wallace, L.M., Kaneko, Y., Hreinsdóttir, S., Hamling, I., Peng, Z., Bartlow, N., D'Anastasio, E. & Fry, B. Large-scale dynamic triggering of shallow slow slip enhanced by overlying sedimentary wedge. *Nature Geoscience* **10**(10), 765–770.

https://doi.org/10.1038/ngeo3021 (2017).

23. Biemiller, J., & Lavier, L. Earthquake supercycles as part of a spectrum of normal fault slip styles. *J. Geophys. Res.* **122**, 3221–3240, doi:10.1002/2016JB013666 (2017).

24. Mortimer, N. & Parkinson, D. Hikurangi Plateau; a Cretaceous large igneous province in the Southwest Pacific Ocean, *J. Geophys. Res.* **101**(B1), 687-696, doi:10.1029/95JB03037 (1996).

25. Barnes, P.M., et al. Tectonic and geological framework for gas hydrates and cold seeps on the Hikurangi subduction margin, *New Zealand. Mar. Geol.* **272**, 26–48 (2010).

26. Ghisetti, F.C., Barnes, P.M., Ellis, S., Plaza-Faverola, A. & Barker, D.H.N. The last 2 Myr of accretionary wedge construction in the central Hikurangi margin (North Island, New Zealand): Insights from structural modelling. *Geochemistry, Geophysics, Geosystems* **17**, 2661–2686, https://doi.org/10.1002/2016GC006341 (2016).

27. Plaza-Faverola, A., Henrys, S., Pecher, I., Wallace, L. & Klaeschen, D. Splay fault branching from the Hikurangi subduction shear zone: Implications for slow slip and fluid flow: *Geochemistry, Geophysics, Geosystems* **17**, p. 5009–5023, https://doi.org/10.1002/2016GC006563 (2016).

28. Darby, D. & Funnell, R.H. Overpressure associated with a convergent plate margin: East Coast Basin, New Zealand. *Pet. Geosci.* **7** (3), 291–299 (2001).

29. Barnes, P.M., Ghisetti, F.C., Ellis, S., & Morgan, J.K. The role of protothrusts in frontal accretion and accommodation of plate convergence, Hikurangi subduction margin, New Zealand. *Geosphere* **14**, (2), 440–468, doi:10.1130/GES01552.1. (2018).

30. Saffer, D.M., Wallace, L.M., Petronotis, K., & the Expedition 375 Scientists. Expedition 375 Preliminary Report: Hikurangi Subduction Margin Coring and Observatories. International Ocean Discovery Program. https://doi.org/10.14379/iodp.pr.375.2018 (2018).

31. Tobin, H.J. & Saffer, D.M. Elevated fluid pressure and extreme mechanical weakness of a plate boundary thrust, Nankai Trough subduction zone. *Geology* **37**, 679–682. http://dx.doi.org/10.1130/G25752A.1 (2009).

32. Moore, C. Tectonics and hydrogeology of accretionary prisms: role of the décollement zone, *J. of Struct. Geol.* **11**, 95-106 (1989).

33. Carson, B. & Screaton, E. Fluid flow in accretionary prisms: evidence for focused, time-variable discharge. *Review of Geophysics* **36** (3), 329-351 (1998).

34. Ando, M., Tu, Y., Kumagai, H., Yamanaka, Y. & Lin, C.-H. Very low frequency earthquakes along the Ryukyu subduction zone. *Geophys. Res. Lett.* **39**, L04303, doi:10.1029/2011GL050559 (2012).

35. Lavier, L. L., Bennett, R. A. & Duddu R. Creep events at the brittle ductile transition, *Geochem. Geophys. Geosyst.* **14**, 3334–3351, doi:10.1002/ggge.20178 (2013).

36. Liu, Y., & Rice, J. R. Aseismic slip transients emerge spontaneously in three-dimensional rate and state modeling of subduction earthquake sequences, *J. Geophys. Res.* **110**, B08307, doi:10.1029/2004JB003424 (2005).

37. Shibazaki, B., & Shimamoto, T. Modelling of short-interval silent slip events in deeper subduction interfaces considering the frictional properties at the unstable-stable transition regime. *Geophysical Journal International* **171**(1), 191–205, https://doi.org/10.1111/j.1365-246X.2007.03434.x (2007).

38. Matsuzawa, T., Hirose, H., Shibazaki, B. & Obara, K. Modeling short- and long-term slow slip events in the seismic cycles of large subduction earthquakes. *J. Geophys. Res.* **115**, B12301 (2010).

39. Liu, Y. Source scaling relations and along-strike segmentation of slow slip events in a 3-D subduction fault model. *Journal of Geophysical Research* **119**, 6512–6533. https://doi.org/10.1002/2014JB011144 (2014).

40. Li, D., & Liu, Y. Spatiotemporal evolution of slow slip events in a nonplanar fault model for northern Cascadia subduction zone, *J. Geophys. Res.* **121**, 6828–6845, doi:10.1002/2016JB012857 (2016).

41. Wei, M., Kaneko, Y., Shi, P. & Liu, Y. Numerical modeling of dynamically triggered shallow slow slip events in New Zealand by the 2016 M_W 7.8 Kaikoura earthquake. *Geophysical Research Letters* **45**, 4764–4772. https://doi.org/10.1029/2018GL077879 (2018).

42. Kitajima, H. & Saffer, D.M. Elevated pore pressure and anomalously low stress in regions of low frequency earthquakes along the Nankai Trough subduction megathrust. *Geophys. Res. Lett.* **39**, L23301. doi:10.1029/2012GL053793 (2012).

43. Araki, E., Saffer, D. M., Kopf, A. J., Wallace, L. M., Kimura, T., Machida, Y., Ide, S., Davis, E., IODP Expedition 365 shipboard scientists. Recurring and triggered slow-slip events near the trench at the Nankai Trough subduction megathrust. *Science* **356**, 1157-1160 (2017).

44. Rubin, A. M., Episodic slow slip events and rate-and-state friction, *J. Geophys. Res.* **113**, B11414, doi:10.1029/2008JB005642 (2008).

45. Rabinowitz, H. S., Savage, H. M., Skarbek, R. M., Ikari, M. J., Carpenter, B. M., & Collettini, C. Frictional behavior of input sediments to the Hikurangi Trench, New Zealand. *Geochemistry, Geophysics, Geosystems* **19**, 2973–2990. https://doi.org/10.1029/2018GC007633 (2018).

46. Ikari, M. J., & Kopf, A. J. Seismic potential of weak, near-surface faults revealed at plate tectonic slip rates. *Science Advances* **3**(11). https://doi.org/10.1126/sciadv.1701269 (2017).

47. Im, K., Saffer, D., Marone, C. & Avouac J.-P. Slip-rate-dependent friction as a universal mechanism for slow slip events. *Nature Geoscience* **13**, 705-710, https://doi.org/10.1038/s41561-020-0627-9 (2020).

48. Li, H., Wei, M., Li, D., Liu, Y., Kim, Y. & Zhou, S. Segmentation of slow slip events in South Central Alaska possibly controlled by a subducted oceanic plateau. *Journal of Geophysical Research* **123**, 418–436. https://doi.org/10.1002/2017JB014911 (2018).

49. Sibson, R. H. Stress switching in subduction forearcs: Implications for overpressure containment and strength cycling on megathrusts. *Tectonophysics* **600**, 142-152 (2013).

50. Warren-Smith, E., Fry, B., Wallace, L., Chon, E., Henrys, S., Sheehan, A., Mochizuki, K., Schwartz, S., Webb, S. & Lebedev, S. Episodic stress and fluid pressure cycling in subducting oceanic crust during slow slip. *Nature Geoscience* **12**(6), 475–481. https://doi.org/10.1038/s41561-019-0367-x (2019).

Acknowledgements

In 2005, seismic line 05CM-38, part of the 05CM survey, was acquired by GNS Science and the New Zealand Ministry of Economic Development. We gratefully acknowledge the captain, technical staff and crew of the *M/V Pacific Titan*. This work was also supported by the Institute for Geophysics at the University of Texas at Austin. SH, DB, IP, LW were supported by the MBIE Endeavour fund Hikurangi subduction earthquakes and slip behavior.

Author contributions

A.F.A. conceived the study and analysed the seismic data. J.B. conducted the rate state friction modeling. A.F.A. and J.B. wrote the manuscript with contributions and edits from all other authors.

Competing interests

The authors declare no competing interests.

Figure Captions:

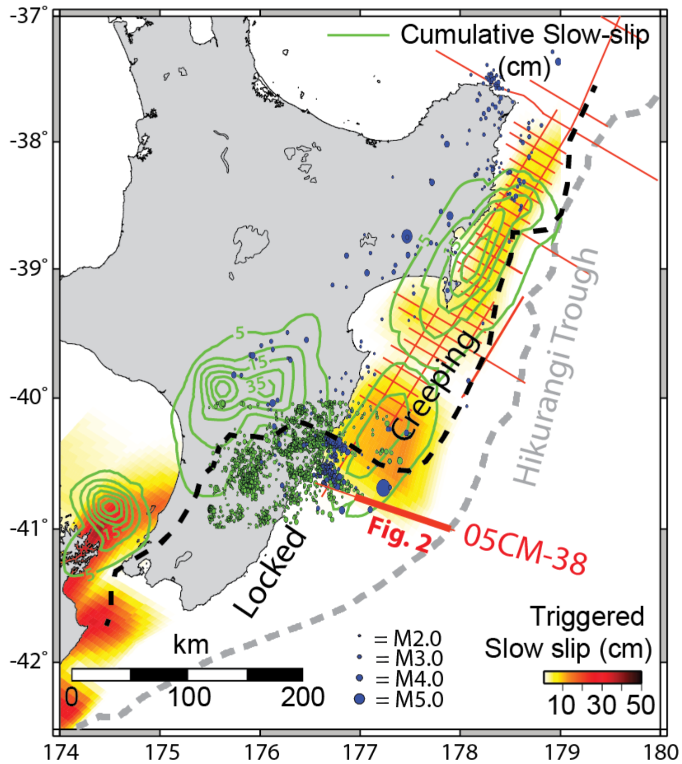

Figure 1 | Tectonic setting and slow slip distribution on the Hikurangi subduction interface. Slow slip on the Hikurangi subduction interface following the M7.8 Kaikoura earthquake[21] (colours, see scale in cm) and cumulative slip in slow-slip events from 2002-2012 (green contours; from ref.[13]). Dashed gray line marks the location of the trench. Dashed black line marks the geodetically determined along-strike transition from an interseismically locked segment in the south to an aseismically creeping segment in the north[13] (i.e. interseismic coupling coefficient = 0.5). The blue circles are earthquakes from the GeoNet catalogue, and the green circles are the repeating earthquakes based on waveform cross-correlation of 17,962 events from 2010-2017[22]. MCS profiles from the 05CM experiment are shown with red lines. Thick red line corresponds to Fig. 2.

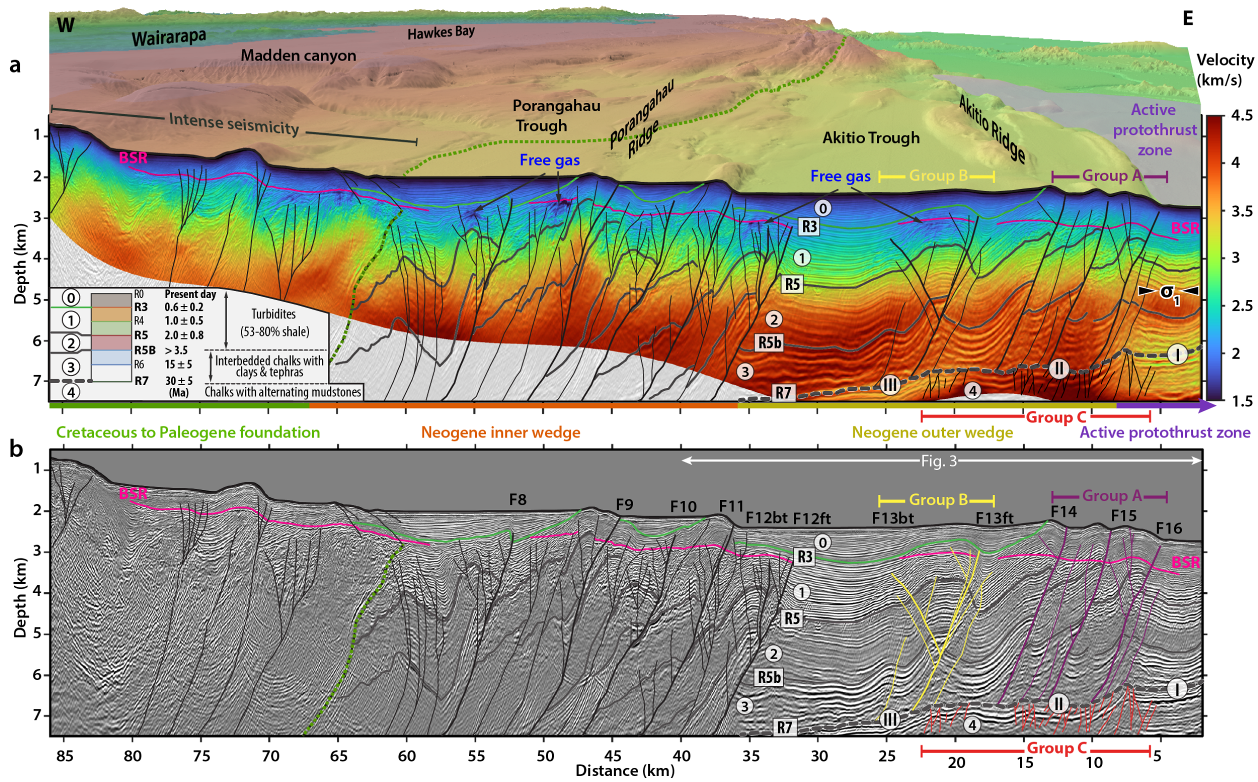

Figure 2 | Seismic structure and geological interpretation across the central Hikurangi margin. a, Composite P-wave velocity and reflectivity model along seismic line 05CM-38 derived from elastic FWI and RTM at a maximum peak frequency of 18-20 Hz (Methods). Marker reflectors (solid green and gray lines) and units (numbered large circles) identified along the seismic line are defined in the inset with their assigned ages[26,27]. Subducted unit 4 below reflector R7, correspond to unit MES and sequence "Y" in refs.[9,26]. The thick dashed gray line marks the megathrust subduction fault. Thick black lines mark major thrust faults and associated frontal thrusts (ft) and back-thrusts (bt)[26,27](labeled on **b)**. Other minor faults are marked with thin black lines. Solid pink lines mark bottom simulating reflections. Regions with contrasting elastic and frictional properties along the subduction fault marked as I, II and III (Extended Data Fig. 6). The dashed green line marks the limit between the Neogene accretionary wedge and the stiffer foundation of pre-subduction Cretaceous marine formations[26]. **b,** Reflectivity image derived from RTM (see Methods). Purple, yellow and red faults on **b** help characterize fault groups A, B and C.

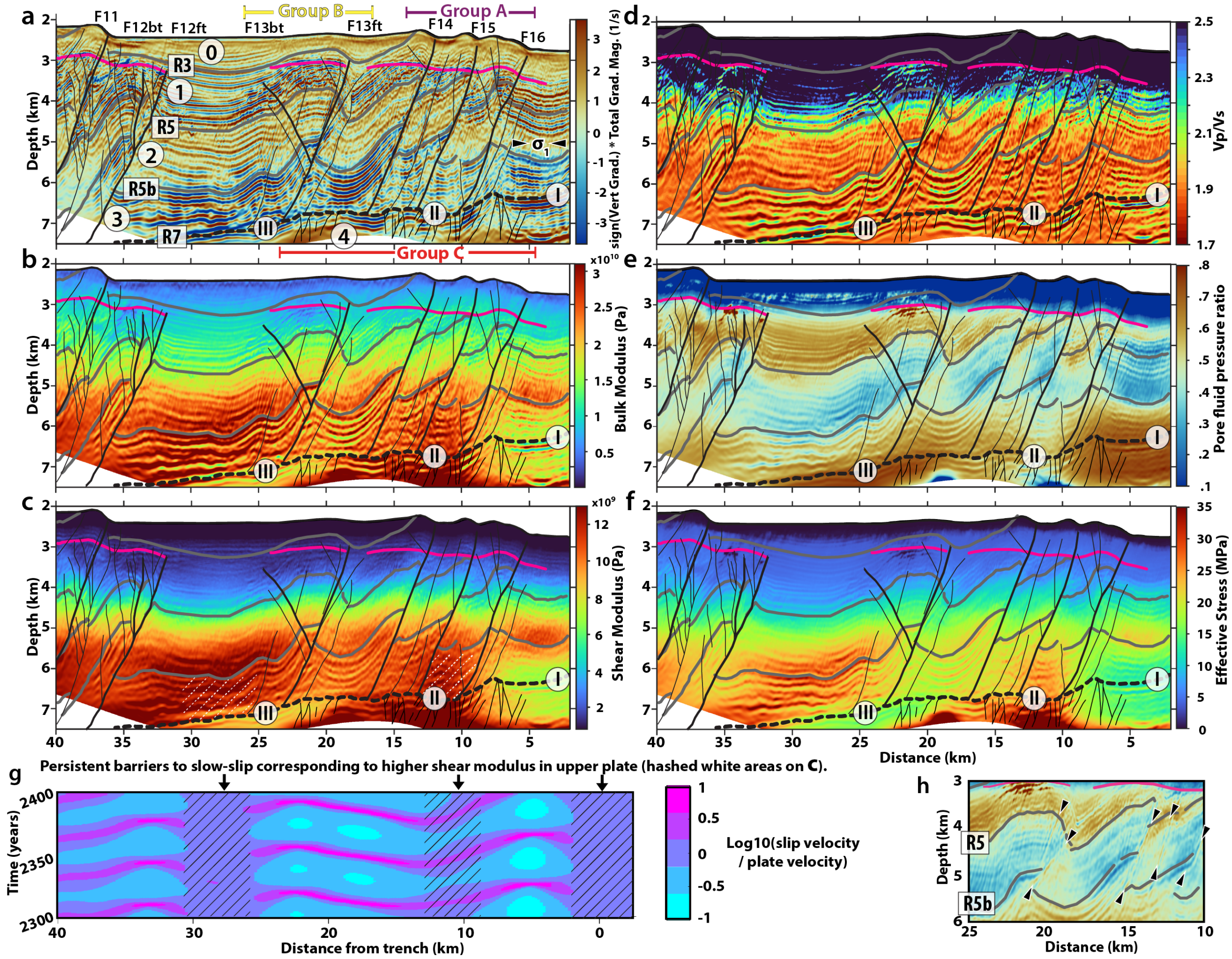

Figure 3 | Physical and mechanical characteristics of the subduction plate boundary and outer Neogene accretionary wedge across the central Hikurangi margin. a, Sign of vertical velocity gradient times the total velocity gradient magnitude (1/s); **b,** bulk modulus; **c,** shear modulus; and **d,** ratio of P-wave to S-wave velocities obtained from elastic FWI (Methods). **e,** Estimated pore fluid pressure ratio and **f,** effective stress estimated from P-wave velocities (Methods). Geological interpretations including markers, reflectors and faults as in Fig. 2. **g,** Slip velocity with time and downdip distance from the trench for a rate-and-state friction continuum model using shear moduli from FWI, constant effective normal stress of 13 MPa, and mildly velocity-weakening b-a = 0.001 (see Methods and Extended Data Fig. 12b). Spontaneous km-scale slow-slip segmentation occurs at local shear modulus maxima (hashed areas on **c** (white) and **g** (black)). **h,** Same as **e** but without the thrust faults.

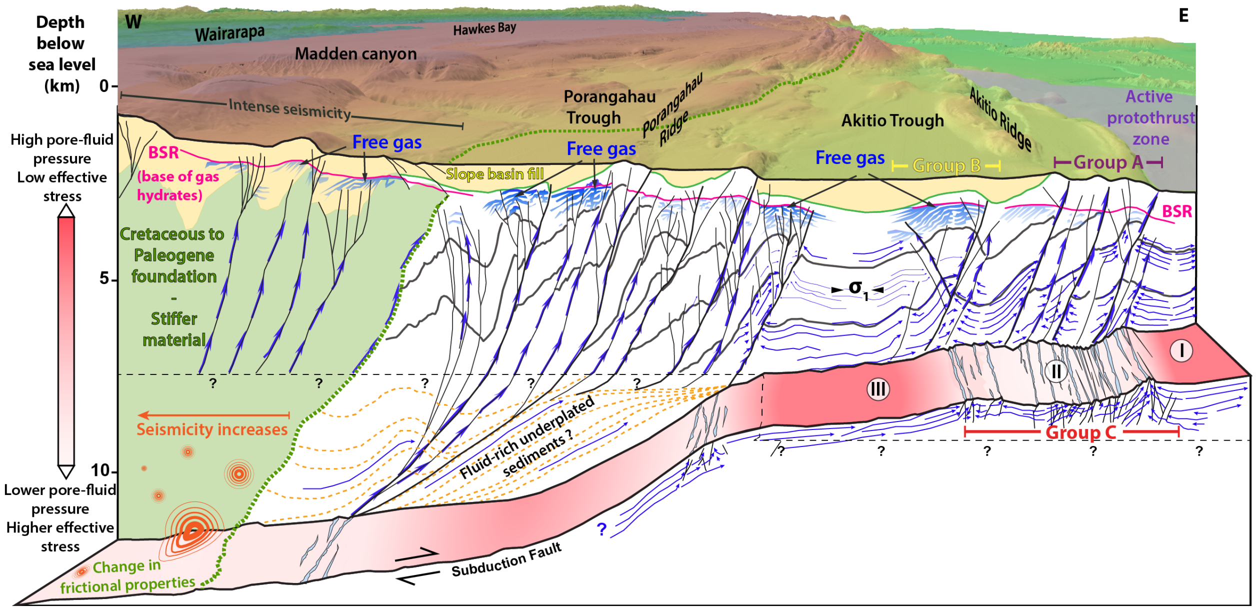

Figure 4 | 3-D conceptual model summarizing several key physical, hydrological and fault slip processes across the central Hikurangi margin. Red shading on the megathrust subduction fault denotes excess pore pressure. Dashed orange lines mark underplated sediments[28]. Blue arrows show proposed fluid flow along higher-permeability strata and thrust faults of high fault permeability. Arrows are scaled qualitatively to illustrate flow rates. Hydrological processes within the footwall and the overriding hanging wall are for the most part independent of each other. Dewatering of the subducted sediments and fluid charging of the strata immediately above the subduction fault appear to be possible in places where faults within the footwall cut through the subduction fault (e.g. group C). As such, thrust fault depressurization of the shallow subduction fault likely influence the size of the regions with contrasting frictional properties along the subduction fault (i.e. regions I, II and III).

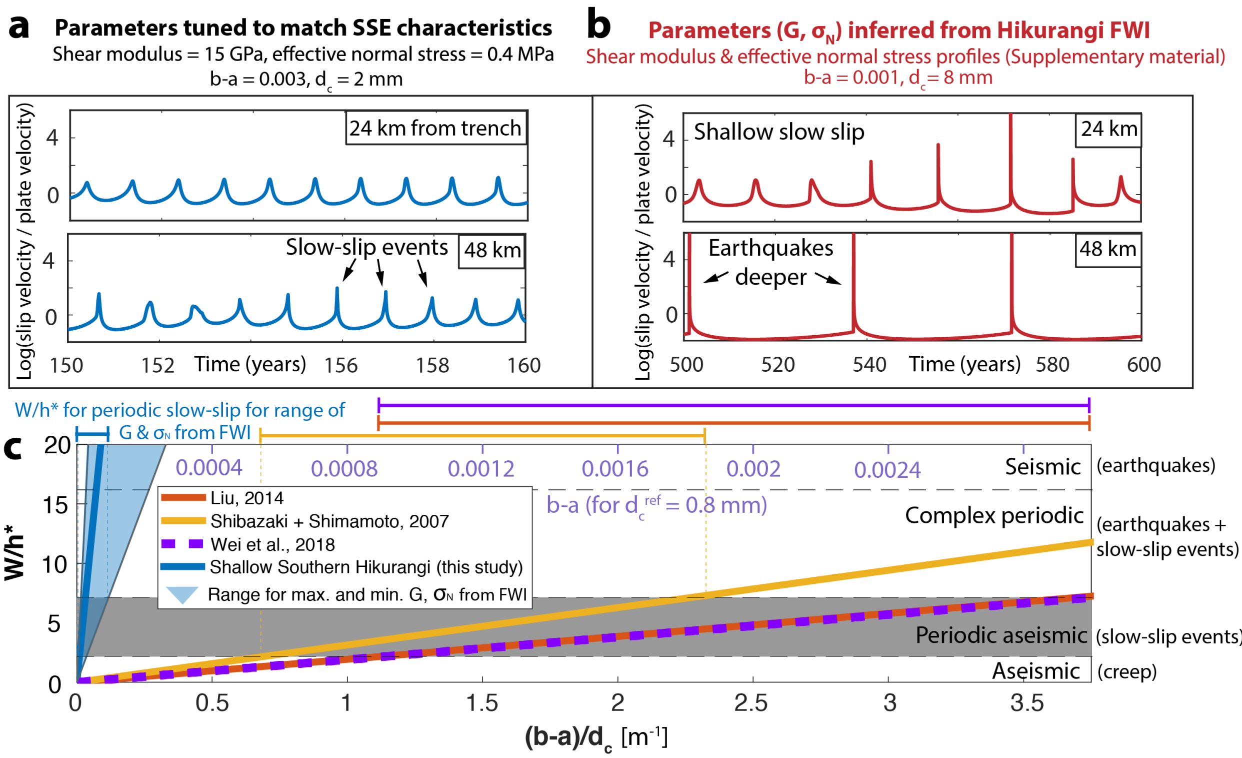

Figure 5 | Rate-state friction model results and stability phase diagram. Slip velocity vs. time for fault patches 24 (upper panel) and 48 (lower panel) km downdip of the trench from models with: **a,** mechanical and frictional parameters tuned to recreate SSE characteristics (after ref.[42]) and, **b,** mechanical properties taken from seismic FWI results from the shallow central Hikurangi margin. The seismically constrained model includes some shallow slow slip (upper panel) but the deeper portion (lower panel) predominantly slips in earthquakes despite a mildly velocity-weakening value of b-a = 0.001. Higher effective normal stress from FWI drives the deeper portions of the modeled fault towards seismic instability, and cannot fully reproduce the recurrence intervals and durations of observed central Hikurangi SSEs, although models with lower (b-a)/d_c approach SSE behavior (**b,** upper panel). **c,** Representative stability regimes for RSF models from various studies. Blue shaded area shows range of stability trajectories based on our seismic inversions (10 MPa < effective stress (σ_N) < 30 MPa; 6 GPa < shear modulus (G) < 14 GPa). Horizontal colored bars show ranges of RSF parameters predicted to allow SSE-type periodic aseismic slip, highlighting the limited range of RSF parameters expected to promote episodic slow-slip for the mechanical conditions inferred from shallow central Hikurangi seismic FWI.

Methods:

Seismic imaging strategy.

Seismic velocity of the subsurface can be separated into two components: (1) a low-frequency component, which affects the travel time, and (2) a high-frequency component which mainly affects the amplitude in the observed seismic signal[51]. A local optimization based full waveform inversion (FWI) can derive some of the high-frequency components but is dependent on the initial model to provide the low-frequency information[52]. Therefore, a kinematically sound initial model is necessary for FWI to converge to a meaningful solution.

To derive a kinematically correct starting model for FWI, we initially performed a linearized traveltime tomographic inversion of a downward extrapolated, 12-km-long offset, multichannel seismic profile following the methodology described in refs.[18-20,53-56].

Downward extrapolation.

Downward extrapolation[57,58] is a technique that can be used to transform seismic field data acquired on the sea surface to a new datum at or near the seafloor, therefore simulating a different acquisition geometry. The resulting dataset is a synthetic ocean-bottom experiment (SOBE[18]). A key advantage of downward extrapolation is that it moves the refracted energy turning just below the seafloor ahead of the seafloor reflection. In this study, we used the Kirchhoff integral formulation of the downward extrapolation operator[57-59] which appropriately accommodates a laterally varying extrapolation datum and non-uniform acquisition geometry.

Processing of the field data was accomplished during the downward extrapolation stage[19]. To minimize the bubble pulse effect, we first applied an optimal predictive deconvolution filter to the observed field data. Second, we applied trace balancing to preserve the continuity of the seismic wavefiled along the streamer. Third, we applied a sixth-order Butterworth band-pass filter with corner frequencies of 3 – 30 Hz to the data. We then convolved the input signal with $H(t)/\sqrt{t}$ (with H the Heaviside step function and t the time) to help better simulate a 2-D experiment and boost low frequencies with respect to high frequencies. The downward extrapolated shot gathers had sources moved to the nearest node of a 12.5 m grid, and 960 evenly spaced receivers starting 12.5 m behind the source and extending to 12 km. The seismic energy was moved to a simulated datum 75 m above the seafloor.

Traveltime tomography.

Traveltimes of downward extrapolated first arrival P-wave refractions as well as reflections from the plate interface reflector were picked along 05CM-38 seismic line, for every fifth SOBE shot gather, representing a total of 327,632 picked traveltimes. The starting P-wave velocity model for tomographic inversion was a smooth version of the velocity structure from ref.[27].

We followed the inversion strategy of refs.[18,54,56]. Forward calculation of travel-time arrivals was done using a shortest path method[60]. The inversion sought to obtain the smoothest velocity model that fits the data within the assigned pick uncertainties. The goodness of the fit between observed (i.e. picked, T_{obs}) and synthetically calculated (T_{syn}) traveltimes was measured by the χ^2 value:

$$\chi^2 = \frac{1}{N}\sum_{i=1}^{N}\frac{(T_{obs,i} - T_{syn,i})^2}{\sigma_{err,i}}, \quad (1)$$

Where σ_{err} is a pick uncertainty (here, 12 ms) and N is the total number of picks. Models were iteratively updated by minimizing a least squares cost function that penalizes a combination of data misfit and model regularization. Our regularization operator penalized the first and second order derivatives (gradient and curvature) of the velocity structure. Horizontal derivatives were given a weight 4 times larger than vertical derivatives owing to the fact that the final seismic velocity structure is expected to be rougher in the vertical direction. Our final model fit the picked arrivals with a ~8 ms root-mean-square traveltime misfit (Supplementary Video 1).

Elastic Full Waveform Inversion (FWI).

Theoretical background

The goal of FWI is to minimize the data residuals $\delta\mathbf{u} = \mathbf{u}^{\mathrm{mod}} - \mathbf{u}^{\mathrm{obs}}$ between the modelled data $\mathbf{u}^{\mathrm{mod}}$ and the observed data $\mathbf{u}^{\mathrm{obs}}$ to estimate the distribution of the material parameters $\mathbf{m}$ in the subsurface. The misfit is measured by the objective function[61,62]:

$$S = \frac{1}{2}\delta\mathbf{u}^{T}\delta\mathbf{u} \tag{2}$$

The term $\delta\mathbf{u}^{\mathbf{T}}\delta\mathbf{u}$ represents the residual energy, i.e. the seismic energy not explained by the actual model $\mathbf{m}$. The objective function is minimized by updating the model parameters $\mathbf{m}$ at each iteration n using a steepest-descent gradient method:

$$\boldsymbol{m}_{n+1} = \boldsymbol{m}_n - \alpha_n \left(\frac{\partial S}{\partial \boldsymbol{m}}\right)_n, \tag{3}$$

where $(\partial S/\partial \mathbf{m})_{\mathrm{n}}$ is the gradient direction of the objective function with respect to the material parameters and α_{n} the step length. According to refs.[14,61,62,63] the gradients for each elastic parameter can be expressed in time domain by a zero-lag correlation of displacement wavefields.

$$\frac{\partial S}{\partial \lambda} = -\sum_{shots}\int \mathrm{d}t \left(\frac{\partial \overrightarrow{u_x}}{\partial \mathrm{x}} + \frac{\partial \overrightarrow{u_z}}{\partial \mathrm{z}}\right)\left(\frac{\partial \overleftarrow{u_x}}{\partial \mathrm{x}} + \frac{\partial \overleftarrow{u_z}}{\partial \mathrm{z}}\right) \tag{4}$$

$$\frac{\partial S}{\partial \mu} = -\sum_{shots}\int \mathrm{d}t \left[2\left(\frac{\partial \overrightarrow{u_x}}{\partial \mathrm{x}}\frac{\partial \overleftarrow{u_x}}{\partial \mathrm{x}} + \frac{\partial \overrightarrow{u_z}}{\partial \mathrm{z}}\frac{\partial \overleftarrow{u_z}}{\partial \mathrm{z}}\right) + \left(\frac{\partial \overrightarrow{u_x}}{\partial \mathrm{z}} + \frac{\partial \overrightarrow{u_z}}{\partial \mathrm{x}}\right)\left(\frac{\partial \overleftarrow{u_x}}{\partial \mathrm{z}} + \frac{\partial \overleftarrow{u_z}}{\partial \mathrm{x}}\right)\right]$$

$$\frac{\partial S}{\partial \rho} = -\sum_{shots}\int \mathrm{d}t \left(\frac{\partial^2 \overrightarrow{u_x}}{\partial \mathrm{t}^2}\overleftarrow{u_x} + \frac{\partial^2 \overrightarrow{u_z}}{\partial \mathrm{t}^2}\overleftarrow{u_z}\right)$$

Where $\rightarrow$ denotes an element of the forward modelled wavefield and $\leftarrow$ denotes an element of the backward propagated data residuals wavefield, generated by propagating the residual data (known as the adjoint wavefield) from the receiver positions backwards in time in the elastic medium. The forward problem and backpropagation of the adjoint wavefield is solved by using a 10^{th} order in space, 2^{nd} order in time, 2-D time domain stress-velocity finite-difference (FD) code[64]. As such, the displacements in equation (4) can be reformulated in terms of stresses and particle velocities[61]:

$$\frac{\partial S}{\partial \lambda} = -\sum_{shots} \int \mathrm{d}t \left[\frac{(\sigma_{xx} + \sigma_{zz})(\Sigma_{xx} + \Sigma_{zz})}{4(\lambda + \mu)^2} \right] \tag{5}$$

$$\frac{\partial S}{\partial \mu} = -\sum_{shots} \int \mathrm{d}t \left[\frac{\sigma_{xz}\Sigma_{xz}}{\mu^2} + \frac{1}{4}\left(\frac{(\sigma_{xx} + \sigma_{zz})(\Sigma_{xx} + \Sigma_{zz})}{(\lambda + \mu)^2} + \frac{(\sigma_{xx} - \sigma_{zz})(\Sigma_{xx} - \Sigma_{zz})}{\mu^2} \right) \right]$$

$$\frac{\partial S}{\partial \rho} = -\sum_{shots} \int \mathrm{d}t \left[v_x \omega_x + v_z \omega_z \right]$$

where σ_{ij} and Σ_{ij} are the stresses and v_i and ω_i are the particle velocities of the forward and back propagated wavefields, respectively. The gradients in terms of other material parameters m' can then be calculated by simple vector transformation[62].

$$\frac{\partial S(\boldsymbol{m})}{\partial \boldsymbol{m}'} = \frac{\partial S(\boldsymbol{m})}{\partial \boldsymbol{m}} \frac{\partial \boldsymbol{m}}{\partial \boldsymbol{m}'} \tag{6}$$

Using the relationships between P-wave velocity V_p, S-wave velocity V_s, the Lamé parameters λ, μ and density ρ, the gradient for V_p, V_s and ρ_{model} can be written as:

$$\frac{\partial S}{\partial V_p} = 2\rho V_p \left(\frac{\partial S}{\partial \lambda}\right) \tag{7}$$

$$\frac{\partial S}{\partial V_s} = -4\rho V_s \left(\frac{\partial S}{\partial \lambda}\right) + 2\rho V_s \left(\frac{\partial S}{\partial \mu}\right)$$

$$\frac{\partial S}{\partial \rho_{model}} = \left(V_p^2 - 2V_s^2\right)\left(\frac{\partial S}{\partial \lambda}\right) + V_s^2 \left(\frac{\partial S}{\partial \mu}\right) + \left(\frac{\partial S}{\partial \rho}\right)$$

To increase the convergence speed an appropriate preconditioning operator P is applied to the gradient $\partial S/\partial \mathbf{m}$

$$\left(\frac{\partial S}{\partial \boldsymbol{m}}\right)_n^p = P_n \left(\frac{\partial S}{\partial \boldsymbol{m}}\right)_n \tag{8}$$

Our preconditioning operator is an approximation to the spatial form of the diagonal of the inverse Hessian (see ref.[65]), which removes the geometrical spreading from the forward and back propagated wavefields and therefore rebalances the contributions of deep and shallow scatters in the gradients.

To further increase the convergence speed of the objective function, the conjugate gradient direction for iteration steps $n \geq 2$ is calculated

$$\left(\frac{\partial S}{\partial \boldsymbol{m}}\right)_n^c = \left(\frac{\partial S}{\partial \boldsymbol{m}}\right)_n^p + \beta \left(\frac{\partial S}{\partial \boldsymbol{m}}\right)_{n-1}^c, with \left(\frac{\partial S}{\partial \boldsymbol{m}}\right)_1^c = \left(\frac{\partial S}{\partial \boldsymbol{m}}\right)_1^p \tag{9}$$

where the weighting factor

$$\beta^{PR} = \frac{\left(\frac{\partial S}{\partial \boldsymbol{m}}\right)_n^P \cdot \left[\left(\frac{\partial S}{\partial \boldsymbol{m}}\right)_n^P - \left(\frac{\partial S}{\partial \boldsymbol{m}}\right)_{n-1}^P\right]}{\left(\frac{\partial S}{\partial \boldsymbol{m}}\right)_{n-1}^P \cdot \left(\frac{\partial S}{\partial \boldsymbol{m}}\right)_{n-1}^P} \tag{10}$$

by Polak-Ribiére is used[66], and $\beta = max\{0, \beta^{PR}\}$ provides a direction reset automatically. We normalize the material parameters and the gradients before the step length calculation. The optimum step length α_n in equation (3) is estimated by a line search algorithm[67].

It is worth noting, that using a conventional streamer acquisition geometry, refs.[63,68] demonstrated that with this implementation of elastic FWI, the P-wave velocity, S-wave velocity and density models of the subsurface can be successfully reconstructed. Indeed, medium wavelength features of S-wave velocity are recoverable from the wide-angle P-wave amplitude-versus-offset response, exploiting the residual P-wavefield (reflected and transmitted), particularly around the critical angle.

Practical considerations

The P-wave velocity model obtained from the tomographic inversion step was used to constrain the starting models for elastic full waveform inversion (FWI, see refs.[19,20,53,55,61]). We estimated a starting S-wave velocity model using the empirical relationships found in ref.[69]. We followed a multistage FWI strategy alternating between model updates, where we inverted simultaneously for P- and S-wave velocities, and source updates. We did not invert for density, which was updated using empirical relationships with P-wave velocities[70,71]. With our elastic FWI inversion scheme we targeted arrivals in downward extrapolated data whose spectra exhibit only limited offset dependence (Extended Data Fig. 5). As such, we assumed for our elastic FWI that the principal attenuation effects can be incorporated into an optimal source wavelet that is updated as part of the inversion process. In a first stage, we ran 60 iterations of elastic FWI, where we targeted only the wide-angle seismic energy in downward extrapolated data ahead of the seafloor reflection and above the first seafloor multiple (Extended Data Figs. 1b, 2b and 3; Supplementary Video 2). For this first stage, modelling was done on a 12.5 m grid and we followed a sequential frequency inversion strategy from low to high frequencies to reconstruct the models. A Butterworth bandpass filter with 6 poles and corner frequencies of 3-8 Hz, 3-10 Hz, 3-12 Hz and 3-15 Hz was used for iterations 0-8, 8-16, 16-24 and 24-60, respectively. In a second stage, an additional 30 iterations of elastic FWI was performed on a 6.25 m modelling grid and we targeted the reflected energy below the seafloor reflection and above the first seafloor multiple (Extended Data Figs. 1c, 2c and 3; Supplementary Video 3). For those 30 iterations, a Butterworth bandpass filter with 6 poles and corner frequencies of 3-20 Hz, 3-25Hz and finally 3-30 Hz was used. Typically, sources updates[62] were run after each set of ~8–10 model updates. The final dominant frequency of the FWI is ~18-20 Hz, for which a maximum resolution of a quarter dominant wavelength corresponding to ~30 m at 2000 m/s and ~70 m at 5000 m/s.

Elastic Reverse Time Migration (RTM).

Reverse-Time Migration (RTM[19,55,72,73]) is a prestack two-way wave-equation migration technique for accurate imaging in and below areas with large structural and velocity complexities. RTM offers the best accuracy and image fidelity among all seismic imaging methods, it has no dip limitation and it handles extreme lateral velocity variations using all possible arrivals.

Our RTM algorithm implements a modelling scheme similar to the one used for the FWI, with two key differences. First, the "adjoint" back-propagated wavefield correspond to the observed data instead of the data residual. Second, the zero-lag crosscorrelation between the forward propagated source-wavefield and back-propagated receiver wavefield is implemented using a pointing-vector imaging condition with illumination compensation and obliquity-correction[74]. The imaging condition optimizes the match between the two wavefields in order to generate the output reflectivity image. In other words, the imaging condition dictates the quality and fidelity of the final RTM image.

Porosity, pore-fluid pressure and effective stress prediction.

We follow an approach similar to that of refs.[10,31,75,76] to derive the state of stress within the accretionary wedge from seismic P-wave velocities obtained from FWI.

To proceed, we first estimate a porosity-depth profile at a reference site seaward of the deformation front using Athy's relationship[77]:

$$\varphi = \varphi_0 \, exp(-\beta z), \tag{11}$$

where φ_0 is the initial porosity of the material at the seafloor, β is the rock compaction coefficient (i.e. 1/compaction length scale) and z is depth (m). The best fitting parameters for the Hikurangi margin are φ_0 = 0.525 and β = 1/3000 = 0.000333 (similar to ref.[76], and validated by recent drilling constraints[78]).

With these parameters, we use equation (5) in ref.[75] to calculate the vertical effective stress (σ_z'), defined as:

$$\sigma_z' = \frac{(\rho_s - \rho_f)g}{\beta}[(\ln \varphi_0 - \varphi_0) - (\ln \varphi - \varphi)], \tag{12}$$

where g is the gravitational acceleration (m.s^{-2}), and ρ_s and ρ_f are the solid grain and fluid densities (kg.m^{-3}), respectively. The best fitting parameters for the Hikurangi margin are $\rho_s = 2740\, kg.m^{-3}$ and $\rho_f = 1030\, kg.m^{-3}$ (from ref.[76]). At the reference site (i.e. seaward of the deformation front), the sediments are under normal consolidation conditions ($\sigma_1' > \sigma_2' = \sigma_3'$, $\sigma_z' = \sigma_1'$, where σ_1', σ_2', and σ_3' are the maximum, intermediate, and minimum principal effective stress, respectively). We then calculate mean effective stress (σ_m') as:

$$\sigma'_m = \frac{\sigma'_1 + \sigma'_2 + \sigma'_3}{3} = \frac{(1+2R)}{3}\sigma'_z, \quad R = \frac{\sigma'_3}{\sigma'_1}, \tag{13}$$

where R is an experimentally determined ratio between minimum and maximum principal effective stress (R = 0.6, from ref.[76]).

Within the accretionary prism, a porosity-depth model is derived from FWI P-wave velocities using equation (9) in ref.[79], with high-consolidation state and a shale fraction of 0.6 validated from drilling constraints[80]. We then convert the porosity to mean effective stress along the entire transect using the relationship derived at the reference site. We assume a forearc coefficient of friction of $\mu = 0.6$; horizontal maximum principal effective stress; and hence the mean effective stress is a factor of 1.6 times the vertical effective stress within the accretionary prism ($\sigma'_{z,wedge}$):

$$\sigma'_{z,wedge} = \frac{\sigma'_m}{1.6}. \tag{14}$$

From there we derive pore fluid pressure (Pf), by substracting vertical effective stress ($\sigma'_{z,wedge}$) from the lithostatic pressure (Pl):

$$P_f = P_l - \sigma'_{z,wedge}. \tag{15}$$

Finally, the Hubbert-Rubey pore fluid pressure ratio (λ*) is calculated as the ratio of fluid pressure (Pf) minus hydrostatic pressure (Ph) to lithostatic pressure (Pl) minus hydrostatic pressure:

$$\lambda^* = (P_f - P_h) / (P_l - P_h). \tag{16}$$

A λ* of zero means that there is no overpressure (i.e. hydrostatic), and is justified when there is efficient hydrogeological connection through the pore network to the ocean. On the other hand, a λ* of 1 corresponds to full overpressure (i.e. lithostatic), and is justified in the presence of a perfect seal without any hydrofracturation.

Rate-state frictional framework for SSEs

Many slow-slip behaviors have been successfully modeled by numerical simulations of planar and non-planar faults in a rate-state friction (RSF) framework[2,4,36-40,81,82]. RSF constitutive laws describe the time-dependent evolution of friction according to the current slip rate V and the history-dependent state variable θ (e.g, refs.[83,84]). Different RSF laws exist to explain different experimental and observational characteristics of seismic and aseismic slip. In this study we use the single state-variable 'ageing' law[83,84,85] which has been used in previous slow-slip modeling studies[2,4,36,39,40,81] and is considered most appropriate for slip that does not reach large earthquake velocities. The ageing law gives the fault friction μ as:

$$\mu = \mu_0 + a \ln \frac{V}{V_0} + b \ln \frac{V_0 \theta}{d_C} \tag{17}$$

where μ_0 is the steady-state coefficient of friction at reference velocity V_0, a is the direct-effect RSF parameter, b is the evolution-effect RSF parameter, and d_C is the characteristic slip length. The state variable has units of time and represents the time-dependent contact evolution processes. The aging-law state variable evolves according to:

$$\dot{\theta} = 1 - \frac{V\theta}{d_C} \tag{18}$$

The RSF parameters a and b are experimentally determined material properties which control the frictional stability of the fault. For $(b\text{-}a) > 0$, the fault patch is velocity-weakening and potentially seismogenic, whereby an increase in velocity yields a decrease in friction. In contrast, for $(b\text{-}a) < 0$ the fault patch is velocity-strengthening and stable or conditionally stable, whereby an increase in slip velocity is countered by an increase in friction, which arrests unstable slip propagation.

Numerical Methods

We model a planar fault with RSF under plane-strain conditions loaded by an overriding elastic plate of thickness H and shear modulus G moving at plate velocity V. Over each timestep dt, elastic stresses are balanced by fault strength using the typical RSF model assumption that stress matches strength. We solve for the slip velocity that satisfies this relationship, and this velocity is prescribed over the period dt in order to calculate elastic strains at the beginning of the subsequent timestep. Each timestep is adaptively scaled to capture both millisecond-scale seismic slip behavior as well as multi-year inter-event deformation as in ref.[86]. We calculate quasistatic stress balances using the Fast Lagrangian Analysis of Continua (FLAC) algorithm[87], which solves the wave-equation while critically damping the inertial component of motion using inertial mass-scaling. We also implement the standard radiation damping approximation to suppress seismic radiation associated with seismic slip (e.g. refs.[2,86]). Full details of the numerical method used in our models can be found in ref.[23].

Central Hikurangi Model Setup

The central Hikurangi SSE patch extends from at least 12 - 6 km depth beneath the East coast of the North Island of New Zealand[13,22], although the updip limit of SSE slip is not well-constrained due to a lack of seafloor geodetic data in this region. Ocean-bottom pressure gauge data from the September-October 2014 SSE recorded slip near the trench in the northern Hikurangi margin, suggesting that slip in the southern patch may also propagate further updip towards the trench; however, similar experiments have not yet been undertaken in the central Hikurangi margin. Here, we model the trench-perpendicular upper 80 km of the decollement, which extends from the trench to ~13 km depth (Extended Data Fig. 9).

The model assumes plane-strain, but the two-dimensional geometry of the decollement and overriding plate are used to calculate the overburden and thickness of the overriding elastic plate. Effective normal stress on the fault is the difference between the weight of the overlying rock column and the pore-fluid pressure at each point (Extended Data Fig. 9), as inferred from seismic FWI. Each fault patch is loaded at the trench-perpendicular convergence rate of 4 cm/yr by an overriding thin elastic plate with thickness H equal to the depth from the seafloor to the decollement, and shear modulus G equal to the average of the seismologically inferred shear modulus of the upper plate directly above the patch (Extended Data Fig. 9). Fault shear modulus G is equal to the seismologically inferred shear modulus along the decollement as drawn in Figure 2 and Extended Data Figs. 6, 7 and 9.

Laboratory rock mechanical experiments show that $b\text{-}a$ is dependent upon temperature, composition, fluid content, slip velocity, confining pressure and effective normal stress. However, in our model the values of $b\text{-}a$ and d_c are the least well-constrained physical parameters. Therefore, to minimize the effect of $b\text{-}a$ and d_c heterogeneity on the modeled slow-slip events, $b\text{-}a$ is set constant and equal to 0.001 between 6 and 12 km depth, increasing linearly to -0.003 updip and downdip of this region; d_c is constant for all portions of the fault and is set to 2-10 mm as in previous studies (e.g., refs.[41,48]).

Data availability.

All multichannel seismic field data, seismic navigation and acquisition logs from the 05CM experiment are archived with the New Zealand government and freely available at the following address (https://data.nzpam.govt.nz/GOLD/system/). Our final two-dimensional elastic full waveform inversion velocity models[89] (doi: 10.26022/IEDA/330190) can be found on the Marine Geoscience Data System.

Code availability.

The seismic processing and imaging codes associated with this paper are maintained by A.F.A. at the Institute for Geophysics at the University of Texas at Austin (aarnulf@ig.utexas.edu). Some components are available on request.

References (Method):

51. Mora, P. Inversion = migration+ tomography. *Geophysics* **54** (12), 1575–1586 (1989).

52. Neves, F., & Singh, S. C. Sensitivity study of seismic reflection/refraction data. *Geophysical Journal International* **126** (2), 470–476 (1996).

53. Arnulf, A. F., Harding, A., Singh, S., Kent, G., & Crawford, W. Fine-scale velocity structure of upper oceanic crust from full waveform inversion of down- ward continued seismic reflection data at the lucky strike volcano, mid-Atlantic ridge. *Geophysical Research Letters* **39** (8), (2012).

54. Arnulf, A. F., Harding, A., Kent, G., Singh, S., & Crawford, W. Constraints on the shallow velocity structure of the lucky strike volcano, mid-atlantic ridge, from downward continued multichannel streamer data. *Journal of Geophysical Research* **119** (2), 1119–1144 (2014).

55. Arnulf, A. F., Harding, A. J., Kent, G. M., Carbotte, S. M., Canales, J. P., & Nedimovic, M. Anatomy of an active submarine volcano. *Geology* **42** (8), 655–658 (2014).

56. Arnulf, A. F., Harding, A., Kent, G., & Wilcock, W. Structure, seismicity, and accretionary processes at the hot spot-influenced axial seamount on the juan de fuca ridge. *Journal of Geophysical Research* **123** (6), 4618–4646 (2018).

57. Berryhill, J. R. Wave-equation datuming before stack, *Geophysics* **49**, 2064–2066 (1984).

58. Shtivelman, V., & Canning, A. Datum correction by wave-equation extrapolation, *Geophysics* **53**(10), 1311–1322 (1988).

59. Larkin, S. P., & Levander, A. Wave-equation datuming for improving deep crustal seismic images. *Tectonophysics* **264**, 371–379, doi:10.1016/S0040-1951(96)00137-0 (1996).

60. Moser, T. Shortest path calculation of seismic rays. *Geophysics* **56** (1), 59–67 (1991).

61. Shipp, R. M., Singh, S. C. Two-dimensional full wavefield inversion of wide-aperture marine seismic streamer data, *Geophys. J. Int.* **151**(2), 325–344, doi:10.1046/j.1365-246X.2002.01645.x. (2002).

62. Mora, P. Nonlinear two-dimensional elastic inversion of multi offset seismic data, *Geophysics* **52**, 1211–1228 (1987).

63. Kohn, D., De Nil, D., Kurzmann, A., Przebindowska, A. & Bohlen, T. On the influence of model parametrization in elastic full waveform tomography. *Geophys. J. Int*. **191**, 325-345, doi:10.1111/j.1365-246X.2012.05633.x (2012)

64. Kindelan, M., Kamel, A. & Sguazzero, P. On the construction and efficiency of staggered numerical differentiators for the wave equation. *Geophysics* **55**, 107–110 (1990).

65. Causse, E., Mittet, R. & Ursin B. Preconditioning of full-waveform inversion in viscoacoustic media. *Geophysics* **64**(1), 130-145 (1999).

66. Polak, E. Computational methods in optimization: A unified approach. *Academic Press.* (1971).

67. Pica, A., Diet, J. P. & Tarantola, A. Nonlinear inversion of seismic reflection data in a laterally invariant medium. *Geophysics* **55**(3), 284-292 (1990).

68. Sears, T., Singh, S. & Barton, P., Elastic full waveform inversion of multi-component OBC seismic data. *Geophysical Prospecting* **56**, no. 6, 843–862 (2008).

69. Castagna, J.P., Batzle, M.L. & Eastwood, R.L. Relationships between compressional-wave and shear-wave velocities in clastic silicate rocks, *Geophysics,* **50,** 571–581 (1985).

70. Gardner, G.H.F., Gardner, L.W. & Gregory, A.R. Formation velocity and density: the diagnostic basics for stratigraphic traps, *Geophysics,* **39,** 770–780 (1974).

71. Hamilton, E.L. Sound velocity-density relations in sea-floor sediments and rocks, *Acoust. Soc. Am. J.,* **63,** 366–377 (1978).

72. Baysal, E., Kosloff, D.D. & Sherwood, J.W.C. Reverse time migration, *Geophysics,* **48,** 1514–1524 (1983).

73. Carbotte, S.M., Arnulf, A. F., Spiegelman, M., Lee, M., Harding, A., Kent, G., Canales, J.-P., Nedimovic, M. Stacked sills forming a deep melt-mush feeder conduit beneath Axial Seamount: *Geology*, **48**, https:// doi.org/10.1130/G47223.1 (2020).

74. Costa, J. C., Silva Neto, F. A., Alcantara, M. R. M., Schleicher J. & Novais, A. Obliquity-correction imaging condition for reverse time migration. *Geophysics* **74**(3), S57-S66 (2009).

75. Skarbek, R.M. & Saffer, D.M. Pore pressure development beneath the decollement at the Nankai subduction ´ zone: implications for plate boundary fault strength and sediment dewatering. *J. Geophys. Res.* **114**:B07401 (2009)

76. Bassett, D., Sutherland, R. & Henrys, S. Slow wavespeeds and fluid overpressure in a region of shallow geodetic locking and slow slip, Hikurangi subduction margin, New Zealand. *Earth and Planetary Science Letters* **389**, 1-13 (2014).

77. Athy, L.F. Density, porosity, and compaction of sedimentary rocks. *Am. Assoc. Pet. Geol. Bull.* **14**, 1–22 (1930).

78. Barnes, P. M., *et al*. Hikurangi Subduction Margin Coring, Logging, and Observatories. Proceedings of the International Ocean Discovery Program, 372B/375: College Station, TX (International Ocean Discovery Program). https://doi.org/10.14379/iodp.proc.372B375.105.2019 (2019)

79. Erickson, S.N. & Jarrard, R.D. Velocity–porosity relationships for water-saturated siliciclastic sediments. *J. Geophys. Res.* **103**, 30385–30406 (1998).

80. Saffer, D., *et al.*, Hikurangi Subduction Margin Coring, Logging, and Observatories. Proceedings of the International Ocean Discovery Program, 372B/375: College Station, TX (International Ocean Discovery Program). https://doi.org/10.14379/iodp.proc.372B375.101.2019 (2019)

81. Liu, Y., & Rice, J. R. Slow slip predictions based on granite and gabbro friction data compared to GPS measurements in northern Cascadia, *J. Geophys. Res.* **114**, B09407, doi:10.1029/2008JB006142 (2009).

82. Shibazaki, B., Bu, S., Matsuzawa, T. & Hirose, H. Modeling the activity of short-term slow slip events along deep subduction interfaces beneath Shikoku, southwest Japan, *J. Geophys. Res.* **115**, B00A19, doi:10.1029/2008JB006057. (2010).

83. Dieterich, J. H. Modeling of rock friction: 1. Experimental results and constitutive equations. *J. Geophys. Res.*, **84**(B5), 2161–2168, doi:10.1029/JB084iB05p02161 (1979).

84. Dieterich, J. H. Constitutive Properties of Faults With Simulated Gouge, in *Mechanical Behavior of Crustal Rocks: The Handin Volume*, edited by N. L. Carter, M. Friedman, J. M. Logan, and D. W. Stearns, pp. 103–120, American Geophysical Union (1981).

85. Ruina, A. Slip instability and state variable friction laws, *J. Geophys. Res.*, **88**(B12), 10359–10370, doi:10.1029/JB088iB12p10359 (1983).

86. Lapusta, N., & Liu, Y. Three-dimensional boundary integral modeling of spontaneous earthquake sequences and aseismic slip. *J. Geophys. Res.* **114**, B09303, doi:10.1029/2008JB005934. (2009).

87. Cundall, P. A. Numerical experiments on localization in frictional materials, *Ing. Arch.* **59**(2), 148–159, doi:10.1007/BF00538368. (1989).

88. Brocher, T. Empirical relations between elastic wavespeeds and density in the Earth's crust. *Bulletin of seismological society of America* **95**(6), 2081-2092, doi:10.1785/0120050077 (2005).

89. Arnulf, A. F. Two-dimensional P-wave and S-wave velocity models of the central Hikurangi convergent margin, New Zealand. *IEDA.,* doi:10.26022/IEDA/330190 (2021).